Materials Today Physics 21 (2021) 100505

Contents lists available at ScienceDirect

Materials Today Physics

journal homepage: https://www.journals.elsevier.com/materials-today-physics

Band convergence and nanostructure modulations lead to high thermoelectric performance in $SnPb_{0.04}Te$-y% $AgSbTe_2$

HPSTAR 1298-2021

Tao Hong [a], Dongyang Wang [a], Bingchao Qin [a], Xiao Zhang [a], Yongjin Chen [b], Xiang Gao [b, **], Li-Dong Zhao [a, *]

[a] School of Materials Science and Engineering, Beihang University, Beijing, 100191, China
[b] Center for High Pressure Science and Technology Advanced Research (HPSTAR), Beijing, 100094, China

ARTICLE INFO

Article history:
Received 14 August 2021
Received in revised form
16 August 2021
Accepted 17 August 2021
Available online 25 August 2021

Keywords:
Thermoelectric materials
SnTe
Band convergence
Nanostructures

ABSTRACT

SnTe is a lead-free and promising mid-temperature thermoelectric material while its performance is largely hindered owing to the relatively high hole carrier concentration originating from the existence of extraordinary Sn vacancies in intrinsic SnTe. In this study, we firstly introduced excess Pb into SnTe matrix to compensate the Sn vacancies, leading to the greatly decreased carrier concentration. Then, we found that the ternary compound $AgSbTe_2$ plays synergistic roles in optimizing the thermoelectric transport properties of SnTe. Namely, alloying $AgSbTe_2$ can induce the electronic band convergence and band flattening in SnTe, leading to the significantly enhanced band effective mass (m^*) and Seebeck coefficient. Additionally, alloying $AgSbTe_2$ produces plentiful Ag-rich nanoprecipitates, which strengthens the scattering of phonons, leading to the lowest lattice thermal conductivity of ~0.47 $Wm^{-1}K^{-1}$. By this stepwise strategy, an outstanding ZT value ~1.1 can be attained at 823 K for the $SnPb_{0.04}Te-12\%AgSbTe_2$ sample, while an average ZT can be obtained ~ 0.72 from 400 K to 800 K for sample $SnPb_{0.04}Te$-12%$AgSbTe_2$. Our study further reveals the great potential for SnTe as promising thermoelectrics.

© 2021 Elsevier Ltd. All rights reserved.

1. Introduction

Thermoelectric (TE) material is a kind of new energy material that can realize the mutual conversion between electricity and heat through the transport of holes and electrons, which can be widely applied in electricity generation and device cooling [1–5]. The property of a TE material is judged by the equation: $ZT = \sigma S^2 T/(\kappa_{ele}+\kappa_{lat})$, where the S denotes the Seebeck coefficient, σ is the electrical conductivity, T represents the absolute temperature in Kelvin, κ_{ele} and κ_{lat} stand for the electronic and lattice thermal conductivity [6,7].

SnTe, as an environmental-friendly compound without Pb, is regarded as an alternative of PbTe owing to the same crystal structure and similar energy band structure [8,9]. Unfortunately, the intrinsic plentiful Sn vacancies make the SnTe possess much inferior thermoelectric property owing to the exorbitant κ_{tot}, extremely high carrier concentration and very low Seebeck coefficient [8,10,11]. In previous study, many attempts have been conducted to optimize the hole carrier concentration, such as self-compensating Sn vacancy [10,12] and inducing Bi [13] and Sb [14] for reversely doping. Moreover, several special chemical elements are verified to enable the convergence of valence bands, resulting in an enhancement in effective mass (m^*) and an improvement in Seebeck coefficient in SnTe, such as Cd [10,15], Mn[16-22], Hg [23–25], Mg[26,27], and Ca [28], *etc.* For thermal transports, there are also various strategies to enhance the decrease of thermal conductivity by inducing point defects [29–31], dense dislocations [12,32,33], and nanoprecipitates [10,34,35] to strength the phonon scattering [36].

$AgSbTe_2$ has a very low thermal conductivity (κ_{lat} ~ 0.47 W m^{-1} K^{-1} at 300 K) and possesses huge thermoelectric potential [37–40], and previous studies have shown that alloying $AgSbTe_2$ has multiple effects in optimizing the thermoelectric performance for both PbTe (LAST) [41] and GeTe (TAGS) [42,43] systems, such as, decreasing the thermal conductivity without

* Corresponding author.
** Corresponding author.
E-mail addresses: hongtao77@buaa.edu.cn (T. Hong), wangdongyang@buaa.edu.cn (D. Wang), qinbingchao@buaa.edu.cn (B. Qin), zhang_xiao@buaa.edu.cn (X. Zhang), yongjin.chen@hpstar.ac.cn (Y. Chen), xiang.gao@hpstar.ac.cn (X. Gao), zhaolidong@buaa.edu.cn (L.-D. Zhao).

https://doi.org/10.1016/j.mtphys.2021.100505
2542-5293/© 2021 Elsevier Ltd. All rights reserved.

affecting the carrier mobility in GeTe-$AgSbTe_2$[43]; adjusting the position of the Fermi surface and promoting the band flattening, meanwhile, increasing the carrier concentration and improving the effective mass of the density of states in SnSe−$AgSbTe_2$[44]; declining the total thermal conductivity by modulating the sizes and distributions of the $AgSbTe_2$-nanoprecipitates in PbTe−$AgSbTe_2$[41]. In addition, it is generally believed that Ag and Sb are in random arrangements in the cationic positions in $AgSbTe_2$ [37,45–47], and it is reasonable to assume that it will have similar effects when alloying $AgSbTe_2$ into other cubic systems, in which multiple cations are distributed randomly in the cationic positions to generate massive point defects. In SnTe−$AgSbTe_2$ system, the low κ_{lat} was achieved because of the lattice softening and phonon-vacancy scattering [48]. In this work, with helping of compensating Sn vacancies using Pb, it is expected that lower κ_{tot} and more superior TE properties can be realized in Pb fulled SnTe−$AgSbTe_2$ system with nanoscale precipitates.

In this study, we firstly introduce additional Pb to compensate the Sn vacancies in SnTe, after which we further induce the low-thermal-conductivity $AgSbTe_2$ to fulfill the synergistic effects in SnTe system. Results illustrate that after exceeding the solid solution limit, $AgSbTe_2$ forms excessive number of second phases as nanoprecipitates in SnTe−$AgSbTe_2$ system, leading to the much-strengthened scattering of the phonons and depressed κ_{lat}. Furthermore, the electrical transports can be simultaneously optimized due to the valence band modulations of band convergence and band flattening induced by $AgSbTe_2$. Finally, we obtained a series of $SnPb_{0.04}Te$-*y*%$AgSbTe_2$ with high thermoelectric performance, further verifying the multiple roles for $AgSbTe_2$ in optimizing the performance of IV-VI thermoelectric systems.

2. Resluts and discussion

Figure S1**(a)** indicates the phase composition analysis of the $SnPb_xTe$ ($x = 0–0.04$) samples. It is obvious that the X-ray diffraction (XRD) results represent a single-phase rock-salt structure ($Fm\bar{3}m$) without any impurity peaks. The lattice parameters increase with rising extra Pb content due to the fact that the ionic radius of Pb atoms (~1.49 Å) is larger than that of Sn atoms (~0.93 Å). The extra Pb atoms can either fill the Sn vacancies or substitute Sn atoms, both of which can result in the expansion of the unit cell, which can be confirmed in Figure S1(b).

Fig. 1 depicts the thermoelectric transport properties changing with temperature of $SnPb_xTe$ ($x = 0–0.04$). As displayed in Fig. 1(a), with temperature rising, the electrical conductivity(σ) for $SnPb_xTe$ keeps falling down. With the increase of extra Pb content, the carrier concentration(n_H) of $SnPb_xTe$ deceases from ~1.63×10^{20} cm^{-3} ($x = 0$) to ~ 5.11×10^{19} cm^{-3} ($x = 0.04$) at room temperature, while the carrier mobility(μ_H) improves from ~305 cm^2 V^{-1} s^{-1}–~877 cm^2 V^{-1} s^{-1}, which is demonstrated in Fig. 1(b). The results illustrate that the extra Pb atoms can successfully compensate Sn vacancies to decline the hole carriers.

The temperature dependence of *S* for $SnPb_xTe$ ($x = 0–0.04$) from 300 K to 823 K is demonstrated in Fig. 1(c), in which the *S* slightly increases from 10.7 μV K^{-1} for Pb-free SnTe to 24.4 μV K^{-1} for $SnPb_{0.04}Te$ at 300 K. Consequently, we achieved the greatly optimized *PF* throughout the temperature range, approaching as high as ~20.6 μW cm^{-1} K^{-2} for the $SnPb_{0.04}Te$ sample at 723 K, as displayed in Fig. 1(d). Meanwhile, owing to the Pb atoms substitution, the κ_{tot} shown in Fig. 1(e) declines from ~8.0 W m^{-1} K^{-1} for Pb-free SnTe to ~ 6.6 W m^{-1} K^{-1} for $SnPb_{0.04}Te$ at 300 K. The reduction of the κ_{tot} mainly derives from the decrease of the κ_{lat}. The thermal diffusivity (*D*), Lorentz number (*L*), thermal capacity (C_p) and κ_{ele} are shown in Figure S2. As demonstrated in Fig. 1(f), enhanced *PF* and reduced κ_{tot} by introducing extra Pb lead to a moderate improvement of *ZT* values, especially for middle temperature range, which is beneficial to obtain larger averaged *ZT*. However, the κ_{tot} of $SnPb_xTe$ is still high, and a further strategy that induces low-thermal-conductivity compound $AgSbTe_2$ is adopted to reduce the κ_{tot} and enhance the thermoelectric performance of $SnPb_{0.04}Te$.

The XRD results for all samples $SnPb_{0.04}Te$-*y*% $AgSbTe_2$ are exhibited in Fig. 2(a). The characteristic peaks of all samples measured by XRD are indexed the same as SnTe with $Fm\bar{3}m$ space group, as labeled below the figure. As the amount of $AgSbTe_2$ rises, the typical peak (200) gradually shifts to higher angle, predicting the reduction of the lattice constant, which is in agreement with the calculated lattice parameters displayed in Fig. 2(b). To maintain the local charge balance, the Ag atoms and Sb atoms are likely to replace the host element Sn by pairs, presenting +1 and + 3 respectively [41]. The decreasing lattice parameters with the increasing $AgSbTe_2$ concentration demonstrate that smaller-size Ag^+ (ionic radius ~ 1.15 Å) and the Sb^{3+} (ionic radius ~ 0.76 Å) effectively incorporate in the Sn^{2+} (ionic radius ~ 0.93 Å) sites.

Moreover, we performed scanning electron microscopy (SEM) measurement and selected a polished surface of the $SnPb_{0.04}Te$-12% $AgSbTe_2$ sample to analyze the distribution of elements, as shown in Figure S3. The various elements (Sn, Te, Pb, Ag, Sb) constituting the sample are uniformly distributed in the micron scale without any obvious second phases.

Fig. 3 depicts the electrical transport properties of $SnPb_{0.04}Te$-*y*% $AgSbTe_2$ from 300 K to 823 K, in which the σ dramatically declines from ~7180 S cm^{-1} in $SnPb_{0.04}Te$ to ~1736 S cm^{-1} in $SnPb_{0.04}Te$-25% $AgSbTe_2$ at 300 K and all σ curves decrease as the temperature rises, exhibiting a typical degenerate semiconductor transport behavior. Figure S4 shows the n_H and μ_H measured at room temperature. While the n_H rises with increasing $AgSbTe_2$ content from ~10^{19} cm^{-3} ($y = 0$) to ~ 10^{21} cm^{-3} ($y = 25$), the corresponding μ_H dramatically falls down from ~877 cm^2 V^{-1} s^{-1} to ~ 9.1 cm^2 V^{-1} s^{-1}. As $AgSbTe_2$ concentration increases, the value of *S* increases from ~24.4 μV K^{-1} for $SnPb_{0.04}Te$ to ~70.9 μV K^{-1} for $SnPb_{0.04}Te$-25% $AgSbTe_2$ at 300 K. Meanwhile, the overall *S* improves with the alloying content throughout entire temperature area and the maximum Seebeck coefficient value reaches approximately 160 μV K^{-1} at 823 K. Due to the higher *S*, the *PF* values are entirely boosted at the whole temperature zone. The *PF* value at 300 K reaches ~10.5 μW cm^{-1} K^{-2} while the peak *PF* ~25.5 μW cm^{-1} K^{-2} at 823 K can be obtained in $SnPb_{0.04}Te$-12% $AgSbTe_2$.

To better understand the ultra-high Seebeck coefficient even with high n_H of ~10^{21} cm^{-3} for the $AgSbTe_2$-alloyed samples, the theoretical Pisarenko plots with different energy offsets (ΔE) based on the two parabolic band model [49,50] are displayed in Fig. 3(d). Obviously, all samples alloyed with $AgSbTe_2$ possess significantly larger *S* than the theoretical value forecasted by the Pisarenko plots even with an extremely low band offset (green line, $\Delta E = 0.05$ eV), indicating the band convergence between the heavy and light valence bands. In addition, the similarly strengthened Seebeck coefficients have been widely discovered in SnTe system doped with In Ref. [49] or alloyed with Cd [10,15], Mn[16-22], Hg [23–25], Mg[26,27], and Ca [28], which has been attributed to the introduction of impurity resonant states or the promotion of band convergence.

In order to clarify the origin of enlarged Seebeck coefficients in SnTe after introducing $AgSbTe_2$, we have performed the first-principles density functional theory (DFT) calculation. Besides, the calculated band structures of $Sn_{27}Te_{27}$, $Sn_{26}AgTe_{27}$ and $Sn_{25}AgSbTe_{27}$ are shown in Fig. 4(a-c). Ag alloying leads to an obvious increment of band gap and flatten of heavy Σ band (Γ-*K* direction) and light *L* band, which is also found for other IV-VI

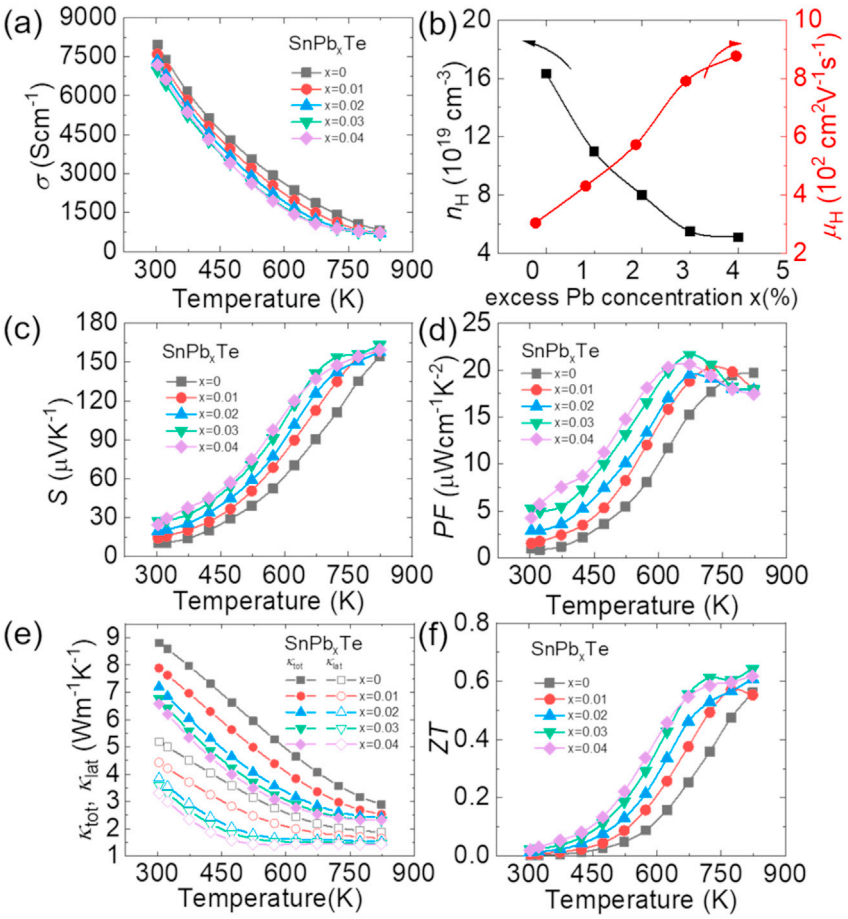

Fig. 1. Thermoelectric performances of the $SnPb_xTe$ ($x = 0–0.04$) samples changing with temperature; including (a) electrical conductivity; (b) carrier concentration and carrier mobility measured at room temperature; (c) the Seebeck coefficient and (d) power factor; (e) total (the solid line) and lattice (the dotted line) thermal conductivity; (f) *ZT*.

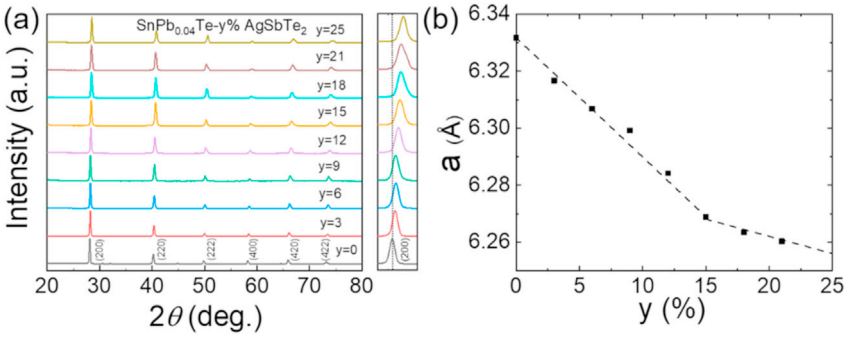

Fig. 2. (a) Powder XRD patterns and the corresponding enlarged area of the peak (200), and (b) lattice parameter for $SnPb_{0.04}Te$-*y*% $AgSbTe_2$ ($y = 0–25$) samples.

semiconductors [51–53]. When Ag and Sb are co-alloyed into SnTe, the band gap becomes more larger and the energy separation turns to be smaller, as displayed in Fig. 4(c). The decrease of ΔE exactly indicates the band convergence of SnTe is caused by alloying $AgSbTe_2$, which is frequently mentioned in previous studies [48,54]. Additionally, after co-alloying Ag and Sb in SnTe, the valence band can be flattened, leading to a sharper increase of density of states (DOS), which is displayed in Fig. 4(d). Both the valence band convergence and band flattening can contribute to the enlarged DOS effective mass m^* by increasing the band degeneracy (N_v) and single-band effective (m_b^*) since $m^* = (N_v)^{2/3} m_b^*$[55]. Therefore, the Seebeck coefficients can be substantially strengthened, leading to much higher *PF* over the whole temperature range.

Fig. 5 depicts the κ_{tot} and κ_{lat} changing with temperature for all $AgSbTe_2$-alloyed samples. κ_{tot} decreases considerably with increasing alloying fraction and it falls down from ~6.57 W m^{-1} K^{-1} for $SnPb_{0.04}Te$ to ~2.04 W m^{-1} K^{-1} for $SnPb_{0.04}Te$-25% $AgSbTe_2$ at 300 K, as shown in Fig. 5(a). Furthermore, a low κ_{tot} of ~1.84 $Wm^{-1}K^{-1}$ is obtained at 823 K. The κ_{lat} can be calculated from subtracting the electronic thermal conductivity (κ_{ele}) from the κ_{tot}: $\kappa_{lat} = \kappa_{tot} - \kappa_{ele}$. The κ_{ele} was calculated by the Weidman-Franz equation: $\kappa_{ele} = L\sigma T$, in which the *L* represents the Lorenz number derived from the Seebeck coefficients [56]. The *D*, *L*, *Cp* and κ_{ele} are

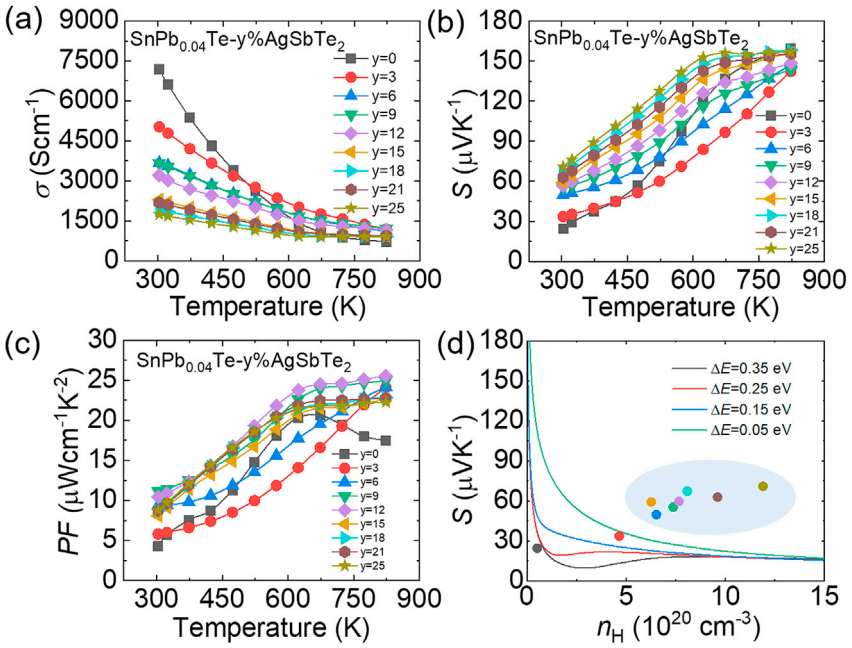

Fig. 3. The properties of electrical transport for $SnPb_{0.04}Te$-*y*% $AgSbTe_2$ ($y = 0$–25). (a) electrical conductivity, (b) Seebeck coefficient, (c) Power factor, (d) the Seebeck coefficient at room temperature as a function of carrier concentration for $SnPb_{0.04}Te$-*y*% $AgSbTe_2$, compared with the theoretical two band Pisarenko curves of SnTe which is indicated by the color line with different energy offset Δ*E*. (For interpretation of the references to color in this figure legend, the reader is referred to the Web version of this article.)

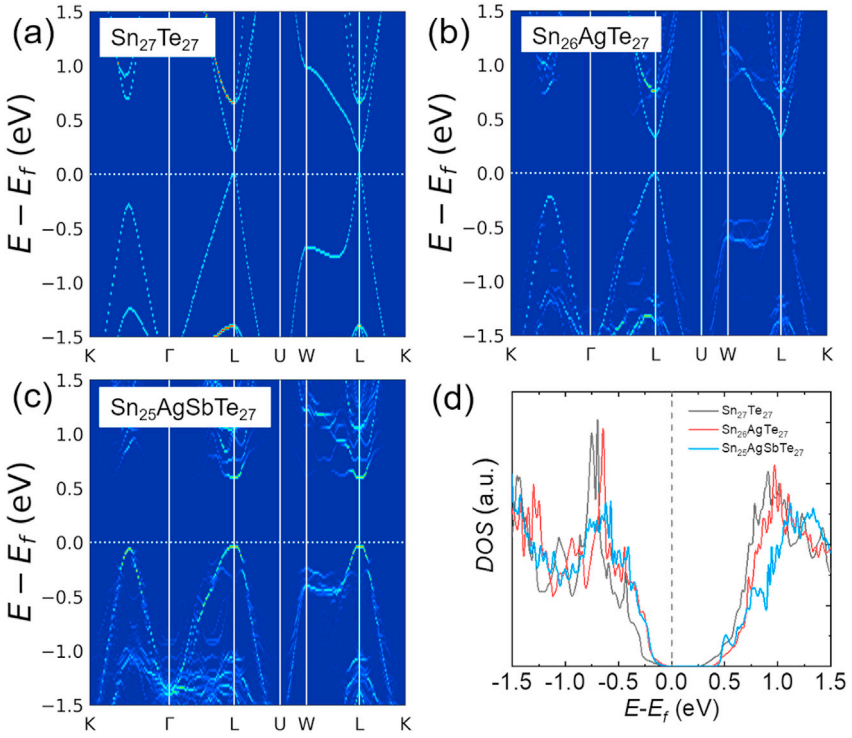

Fig. 4. (a–c) Calculated band structures of $Sn_{27}Te_{27}$, $Sn_{26}AgTe_{27}$ and $Sn_{25}AgSbTe_{27}$ and (d) the density of states (DOS) of $Sn_{27}Te_{27}$, $Sn_{26}AgTe_{27}$ and $Sn_{25}AgSbTe_{27}$.

clearly displayed in Figure S5. As demonstrated in Fig. 5(b), κ_{lat} gradually declines with the rise of alloying fraction, and the minimal κ_{lat} approaches as low as ~ 0.47 W m^{-1} K^{-1} at 823 K in $SnPb_{0.04}Te$-12% $AgSbTe_2$. Therefore, the decrease in κ_{tot} mainly arises from the decrease of κ_{lat}.

To reveal the low κ_{lat} of the $SnPb_{0.04}Te$-y% $AgSbTe_2$ samples, the transmission electron microscopy (TEM) and the scanning transmission electron microscopy (STEM) analysis are conducted. As shown in Fig. 6(a), the formation of considerable nano-precipitates embedded in the SnTe-based matrix is obvious. Fig. 6(b) exhibits various typical ellipsoid-shaped precipitates, and the corresponding selected area electron diffraction (SAED) pattern in Fig. 6(c) matches well with the cubic SnTe ($Fm\bar{3}m$) structure

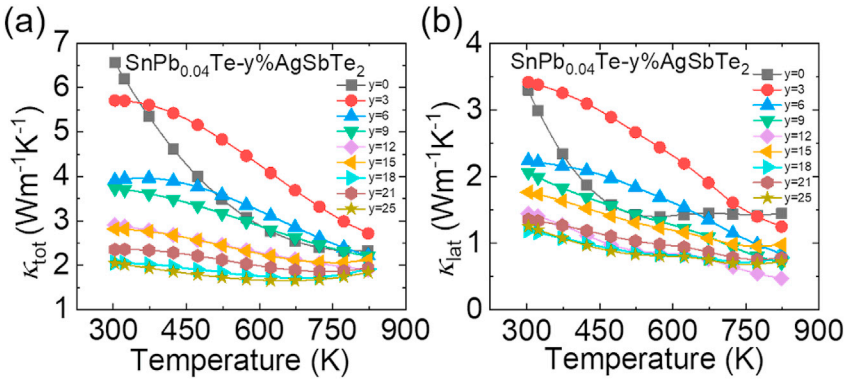

Fig. 5. The thermal conductivity changing as the temperature rises for $SnPb_{0.04}Te$-y% $AgSbTe_2$ ($y = 0–25$): (a) κ_{tot}; (b) κ_{lat}.

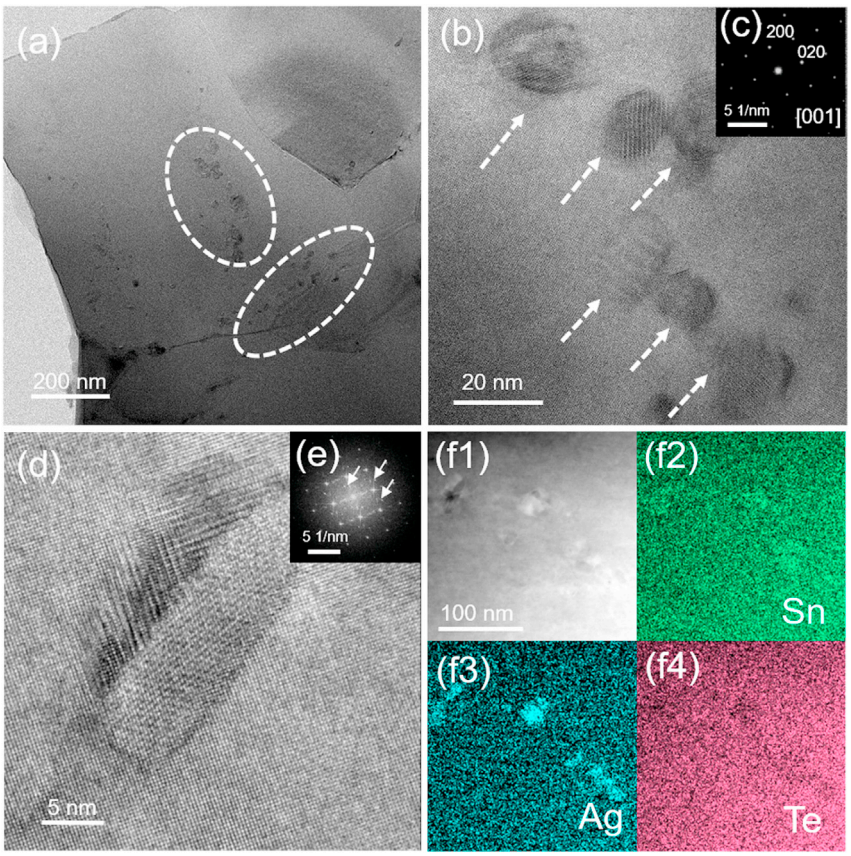

Fig. 6. (a) Bright-field TEM image taken from $SnPb_{0.04}Te$-12% $AgSbTe_2$. (b) Enlarged bright-field TEM image showing the formation of considerable nanoprecipitates (arrowed) as marked also in a). (c) The corresponding selected area electron diffraction (SAED) pattern of b). (d–e) High-resolution TEM (HRTEM) image of a selected nanoprecipitate and its Fast Fourier Transform (FFT) image. (f1) Annular dark-field (ADF) STEM image and (f2-4) corresponding elemental mappings obtained from the STEM energy-dispersive X-ray spectroscopy (EDS).

along its [001] direction. The results indicate that alloying $AgSbTe_2$ retains the crystal structure of SnTe. According to the direct observation, we find the size of the second phase ranges from 10 to 30 nm. From the high-resolution TEM (HRTEM) image shown in Fig. 6(d), it is found the nanoprecipitate shows a different lattice structure from that of the SnTe matrix. As is in good consistence with the HRTEM observation, two series of diffraction spots can be clearly observed from the corresponding Fast Fourier Transform (FFT) image in Fig. 6(e), i.e., the weak spots (arrowed), which correspond to the nanoprecipitates, can be clearly identified from the remain of the matrix that well indexed by [001]-axis projection of the cubic SnTe. Therefore, it is likely that the nanoprecipitate is introduced by the addition of $AgSbTe_2$.

In order to examine the specific chemical composition of the nanoprecipitates, annular dark-field (ADF) STEM imaging and elemental mapping analysis are conducted, as is shown in Fig. 6(f1-f4) and Figure S6. The EDS mappings show that among the constituent elements of the sample, only the Ag is rich in the nanoprecipitates and the other elements are evenly distributed. Based on the results, we propose that alloying $AgSbTe_2$ brings in considerable Ag-rich nanoprecipitates, which is effective in promoting the scattering of high frequency phonons and thus decreasing the κ_{lat}.

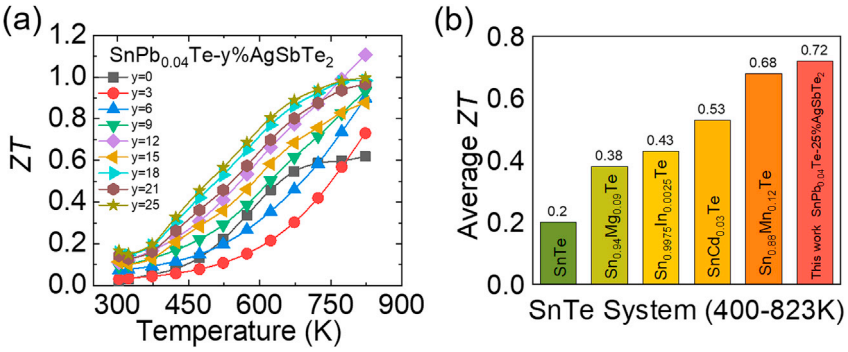

Fig. 7. (a) ZT values of $SnPb_{0.04}Te$-y% $AgSbTe_2$ ($y = 0$–25) and (b) comparison of average ZT (ZT_{ave}) between $SnPb_{0.04}Te$-25% $AgSbTe_2$ in this work and previous works [10,16,26,49].

Owing to the simultaneous optimization of the electrical and thermal properties, the final ZT can be optimized. As demonstrated in Fig. 7(a), a maximum value ~ 1.1 for $SnPb_{0.04}Te$-12% $AgSbTe_2$ at 823 K is obtained. Furthermore, besides the considerable peak ZT values, we also obtain the overall optimized ZT curves over the entire temperature zone, leading to an enlarged average ZT (ZT_{ave}) [57]. The ZT_{ave} is derived from the following equation [57]:

$$ZT_{ave} = \frac{1}{T_h - T_c}\int_{T_c}^{T_h} ZTdT \quad (1)$$

As illustrated in Fig. 7(b), an exciting ZT_{ave} value exceeding 0.72 for $SnPb_{0.04}Te$-25% $AgSbTe_2$ at 400–823 K can be achieved. It is worth noting that the ZT_{ave} is superior to the reported SnTe-based systems, such as ~0.38 for $Sn_{0.94}Mg_{0.09}Te$ [26], ~0.43 for $Sn_{0.9975}In_{0.0025}Te$ [49], ~0.53 for $SnCd_{0.03}Te$ [10] and ~0.68 for $Sn_{0.88}Mn_{0.12}Te$ [16]. This study provides a path to improve the thermoelectric properties by alloying low-thermal-conductivity ternary compound into conventional cubic phase thermoelectric materials and it paves the way for further optimizing the property of thermoelectric material by utilizing the multiple effects.

3. Conclusion

In this work, excess Pb can effectively compensate the Sn vacancies of SnTe to reduce the hole carrier concentration. Alloying $AgSbTe_2$ has multiple effects in optimizing the thermoelectric performances of the $SnPb_{0.04}Te$. Specifically, $AgSbTe_2$ alloying promotes the valence band convergence and flattening, both of which contribute to the enhanced m^* and Seebeck coefficient, resulting in the substantially enlarged average PF. And the presence of the Ag-rich nanoprecipitates effectively strengthen phonon scattering, leading to the dramatic decline in κ_{lat} to ~0.47 W m^{-1} K^{-1} at 823 K. Collectively, a peak ZT ~1.1 is attained in $SnPb_{0.04}Te$-12% $AgSbTe_2$ at 823 K and a maximum ZT_{ave} approaches 0.72 at 400–823 K for $SnPb_{0.04}Te$-25% $AgSbTe_2$. This work offers an effective approach to improve the TE property through synergistically optimizing the PF via tuning electronic band structure and declining the thermal conductivity by the nanostructures.

Author contributions

Tao Hong conceived and carried out the experiments, synthesized the samples, performed the SEM and TEM measurements with the assistance of Yongjin Chen and Xiang Gao and wrote this paper. Dongyang Wang carried out the DFT calculations, conceived the experiments, analyzed the results and co-edited the manuscript. Bingchao Qin conceived the experiments, analyzed the results and co-edited the manuscript. Xiao Zhang analyzed the results and co-edited the manuscript. Xiang Gao and Li-Dong Zhao designed and carried out the experiments, analyzed the results and co-edited the manuscript.

Declaration of competing interest

There are no conflicts of interest to declare.

Acknowledgments

This work was supported by National Natural Science Foundation of China (51772012, 52002042 and 52002011), National Key Research and Development Program of China (2018YFA0702100 and 2018YFB0703600), the Beijing Natural Science Foundation (JQ18004), Shenzhen Peacock Plan team (KQTD20160226195659991) and 111 Project (B17002). This work was also supported by the National Postdoctoral Program for Innovative Talents (BX20200028). This Project was also supported by China Postdoctoral Science Foundation (2021M690280) and Natural Science Foundation of Chongqing, China (cstc2019jcyj-msxmX0554). L.D.Z. appreciates the support of the high-performance computing (HPC) resources at Beihang University, the National Science Fund for Distinguished Young Scholars (51925101), and center for High Pressure Science and Technology Advanced Research (HPSTAR) for SEM and TEM measurements.

Appendix A. Supplementary data

Supplementary data to this article can be found online at https://doi.org/10.1016/j.mtphys.2021.100505.

References

[1] X. Zhang, L.-D. Zhao, J. Materiomics 1 (2015) 92–105.
[2] G. Tan, L.D. Zhao, M.G. Kanatzidis, Chem. Rev. 116 (2016) 12123–12149.
[3] Xiao, Y., and Zhao, L.-D. Science 367 (2020), 1196-1197.
[4] X.-L. Shi, J. Zou, Z.-G. Chen, Chem. Rev. 120 (2020) 7399–7515.
[5] G.J. Snyder, E.S. Toberer, Nat. Mater. 7 (2008) 105–114.
[6] L.-D. Zhao, S.-H. Lo, Y. Zhang, H. Sun, G. Tan, C. Uher, C. Wolverton, V.P. Dravid, M.G. Kanatzidis, Nature 508 (2014) 373–377.
[7] K. Biswas, J. He, I.D. Blum, C.-I. Wu, T.P. Hogan, D.N. Seidman, V.P. Dravid, M.G. Kanatzidis, Nature 489 (2012) 414–418.
[8] R.F. Brebrick, A. Strauss, J. Phys. Rev. 131 (1963) 104–110.
[9] L.M. Rogers, J. Phys. D Appl. Phys. 1 (1968) 845–852.
[10] G. Tan, L.-D. Zhao, F. Shi, J.W. Doak, S.-H. Lo, H. Sun, C. Wolverton, V.P. Dravid, C. Uher, M.G. Kanatzidis, J. Am. Chem. Soc. 136 (2014) 7006–7017.
[11] G. Tan, F. Shi, H. Sun, L.-D. Zhao, C. Uher, V.P. Dravid, M.G. Kanatzidis, J. Mater. Chem. A 2 (2014) 20849–20854.
[12] F. Guo, B. Cui, Y. Liu, X. Meng, J. Cao, Y. Zhang, R. He, W. Liu, H. Wu, S.J. Pennycook, W. Cai, J. Sui, Small 14 (2018) 1802615.
[13] Z.W. Zhou, J.Y. Yang, Q.H. Jiang, Y.B. Luo, D. Zhang, Y.Y. Ren, X. He, J.W. Xin, J. Mater. Chem. A 4 (2016) 13171–13175.

[14] A. Banik, B. Vishal, S. Perumal, R. Datta, K. Biswas, Energy Environ. Sci. 9 (2016) 2011–2019.
[15] J. He, J. Xu, G.-Q. Liu, H. Shao, X. Tan, Z. Liu, J. Xu, H. Jiang, J. Jiang, RSC Adv. 6 (2016) 32189–32192.
[16] G. Tan, F. Shi, S. Hao, H. Chi, T.P. Bailey, L.-D. Zhao, C. Uher, C. Wolverton, V.P. Dravid, M.G. Kanatzidis, J. Am. Chem. Soc. 137 (2015) 11507–11516.
[17] J. He, X. Tan, J. Xu, G.-Q. Liu, H. Shao, Y. Fu, X. Wang, Z. Liu, J. Xu, H. Jiang, J. Jiang, J. Mater. Chem. A 3 (2015) 19974–19979.
[18] H.J. Wu, C. Chang, D. Feng, Y. Xiao, X. Zhang, Y.L. Pei, L. Zheng, D. Wu, S.K. Gong, Y. Chen, J.Q. He, M.G. Kanatzidis, L.D. Zhao, Energy Environ. Sci. 8 (2015) 3298–3312.
[19] W. Li, Z. Chen, S. Lin, Y. Chang, B. Ge, Y. Chen, Y.J. Pei, Materiomics 1 (2015) 307–315.
[20] Z.Y. Chen, B. Gao, J. Tang, X.M. Guo, W. Li, R. Ang, Appl. Phys. Lett. 115 (2019): 073903.
[21] Z. Yao, W. Li, J. Tang, Z. Chen, S. Lin, K. Biswas, A. Burkov, Y. Pei, Infomat 1 (2019) 571–581.
[22] Z. Chen, J. Tang, X. Guo, F. Zhang, M. Tang, F. Xiong, Y. Chen, R. Ang, Appl. Phys. Lett. 116 (2020) 193902.
[23] G. Tan, F. Shi, J.W. Doak, H. Sun, L.-D. Zhao, P. Wang, C. Uher, C. Wolverton, V.P. Dravid, M.G. Kanatzidis, Energy Environ. Sci. 8 (2015) 267–277.
[24] X.J. Tan, H.Z. Shao, J. He, G.Q. Liu, J.T. Xu, J. Jiang, H.C. Jiang, Phys. Chem. Chem. Phys. 18 (2016) 7141–7147.
[25] X. Tan, G. Liu, J. Xu, X. Tan, H. Shao, H. Hu, H. Jiang, Y. Lu, J.J. Jiang, Materiomics 4 (2018) 62–67.
[26] A. Banik, U.S. Shenoy, S. Anand, U.V. Waghmare, K. Biswas, Chem. Mater. 27 (2015) 581–587.
[27] S. Roychowdhury, U.S. Shenoy, U.V. Waghmare, K. Biswas, J. Mater. Chem. C 5 (2017) 5737–5748.
[28] R.A.R. Al Orabi, N.A. Mechosky, J. Hwang, W. Kim, J.-S. Rhyee, D. Wee, M. Fornari, Chem. Mater. 28 (2016) 376–384.
[29] A. Banik, K. Biswas, J. Mater. Chem. A 2 (2014) 9620–9625.
[30] Y. Pei, L. Zheng, W. Li, S. Lin, Z. Chen, Y. Wang, X. Xu, H. Yu, Y. Chen, B. Ge, Adv. Electron. Mater. 2 (2016) 1600019.
[31] H. Liu, X. Shi, F. Xu, L. Zhang, W. Zhang, L. Chen, Q. Li, C. Uher, T. Day, G. Snyder, J. *Nat. Mater.* 11 (2012) 422–425.
[32] X. Xu, L. Xie, Q. Lou, D. Wu, J. He, Adv. Sci. 5 (2018) 1801514.
[33] D. Wu, X. Chen, F.S. Zheng, H.C. Du, L. Jin, R.E. Dunin-Borkowski, ACS Appl. Energy Mater. 2 (2019) 2392–2397.
[34] J. Hwang, H. Kim, M.-K. Han, J. Hong, J.-H. Shim, J.-Y. Tak, Y.S. Lim, Y. Jin, J. Kim, H. Park, D.-K. Lee, J.-H. Bahk, S.-J. Kim, W. Kim, ACS Nano 13 (2019) 8347–8355.
[35] M. Hong, Y. Wang, S. Xu, X. Shi, L. Chen, J. Zou, Z.-G. Chen, Nanomater. Energy 60 (2019) 1–7.
[36] Qin, B., Wang, D., Zhao, L. D. InfoMat 3 (2021), 755-789.
[37] J. Ma, O. Delaire, A.F. May, C.E. Carlton, M.A. McGuire, L.H. VanBebber, D.L. Abernathy, G. Ehlers, T. Hong, A. Huq, W. Tian, V.M. Keppens, Y. Shao-Horn, B.C. Sales, Nat. Nanotechnol. 8 (2013) 445–451.
[38] J. Ma, O. Delaire, E.D. Specht, A.F. May, O. Gourdon, J.D. Budai, M.A. McGuire, T. Hong, D.L. Abernathy, G. Ehlers, E. Karapetrova, Phys. Rev. B 90 (2014) 134303.
[39] D.T. Morelli, V. Jovovic, J.P. Heremans, Phys. Rev. Lett. 101 (2008): 035901.
[40] Roychowdhury, S., Ghosh, T., Arora, R., Samanta, M., Xie, L., Singh, N. K., Soni, A., He, J., Waghmare, U. V., Biswas, K. Science 371 (2021), 722-727.
[41] K.F. Hsu, S. Loo, F. Guo, W. Chen, J.S. Dyck, C. Uher, T. Hogan, E.K. Polychroniadis, M.G. Kanatzidis, Science 303 (2004) 818–821.
[42] S.K. Placheova, Phys. Status Solidi A 83 (1984) 349–355.
[43] S.H. Yang, T.J. Zhu, T. Sun, J. He, S.N. Zhang, X.B. Zhao, Nanotechnology 19 (2008) 245707.
[44] H. Wang, H. Hu, N. Man, C. Xiong, Y. Xiao, X. Tan, G. Liu, Jiang, J. *Mater. Today Phys.* 16 (2021) 100298.
[45] E. Quarez, K.-F. Hsu, R. Pcionek, N. Frangis, E.K. Polychroniadis, M.G. Kanatzidis, J. Am. Chem. Soc. 127 (2005) 9177–9190.
[46] S.V. Barabash, V. Ozolins, C. Wolverton, Phys. Rev. Lett. 101 (2008) 155704.
[47] K. Hoang, S.D. Mahanti, J.R. Salvador, M.G. Kanatzidis, Phys. Rev. Lett. 99 (2007) 156403.
[48] G. Tan, S. Hao, R.C. Hanus, X. Zhang, S. Anand, T.P. Bailey, A.J.E. Rettie, X. Su, C. Uher, V.P. Dravid, G.J. Snyder, C. Wolverton, M.G. Kanatzidis, ACS Energy Lett. 3 (2018) 705–712.
[49] Q. Zhang, B. Liao, Y. Lan, K. Lukas, W. Liu, K. Esfarjani, C. Opeil, D. Broido, G. Chen, Z. Ren, Proc. Natl. Acad. Sci. U.S.A. 110 (2013) 13261–13266.
[50] X. Zhang, D. Wang, H. Wu, M. Yin, Y. Pei, S. Gong, L. Huang, S.J. Pennycook, J. He, L.-D. Zhao, Energy Environ. Sci. 10 (2017) 2420–2431.
[51] Y. Pei, A.D. LaLonde, H. Wang, G.J. Snyder, Energy Environ. Sci. 5 (2012) 7963–7969.
[52] I.I. Ravich, Semiconducting Lead Chalcogenides, Springer Science & Business Media, 2013.
[53] Y. Xiao, H.J. Wu, J. Cui, D.Y. Wang, L.W. Fu, Y. Zhang, Y. Chen, J.Q. He, S.J. Pennycook, L.D. Zhao, Energy Environ. Sci. 11 (2018) 2486–2495.
[54] Y. Chen, M.D. Nielsen, Y.B. Gao, T.J. Zhu, X.B. Zhao, J.P. Heremans, Adv. Energy Mater. 2 (2012) 58–62.
[55] Y. Pei, X. Shi, A. LaLonde, H. Wang, L. Chen, G.J. Snyder, Nature 473 (2011) 66–69.
[56] L.D. Zhao, S.H. Lo, J. He, H. Li, K. Biswas, J. Androulakis, C.I. Wu, T.P. Hogan, D.Y. Chung, V.P. Dravid, M.G. Kanatzidis, J. Am. Chem. Soc. 133 (2011) 20476–20487.
[57] B. Qin, Y. Zhang, D. Wang, Q. Zhao, B. Gu, H. Wu, H. Zhang, B. Ye, S.J. Pennycook, L.-D. Zhao, J. Am. Chem. Soc. 142 (2020) 5901–5909.